

# 3-D High-Resolution Imaging and Array Calibration of Ground-Based Millimeter-Wave MIMO Radar

Gang Xu<sup>1D</sup>, Senior Member, IEEE, Yuzhi Chen, Student Member, IEEE, Ang Ji<sup>1D</sup>, Student Member, IEEE, Bangjie Zhang<sup>1D</sup>, Student Member, IEEE, Chao Yu<sup>1D</sup>, Senior Member, IEEE, and Wei Hong<sup>1D</sup>, Fellow, IEEE

**Abstract**—Ground-based (GB) radar imaging can provide mapping of interesting terrains and accurately monitor deformation in a noncontact manner, which has found a wide application in landslide warning and so on. In this article, a novel 3-D synthetic aperture radar (SAR) imaging and array phase error calibration algorithm is proposed using the micro multiple-input–multiple-output (MIMO) millimeter-wave (mmW) radar sensor. The framework of Doppler-division multiplexing (DDM) MIMO-SAR is designed to be suitable for a moving platform, i.e., a rail-mounted-based radar system. Then, a novel 3-D SAR imaging algorithm is presented to integrate the backprojection (BP) 2-D imaging and super-resolution MIMO array imaging by using an atomic norm minimization (ANM) method. Benefiting from the off-grid characteristic of atomic norm, the proposed ANM 3-D SAR imaging algorithm can effectively overcome the drawback of discrete errors compared with conventional methods using the discrete dictionary of Fourier transform. Meanwhile, a minimum entropy algorithm is proposed to accurately estimate and correct the MIMO array phase errors, which is classified as the self-calibration method. Finally, the numerical experiments using the measured data from a 77-GHz  $4 \times 8$  radar are performed to confirm the proposed GB 3-D SAR imaging algorithm.

**Index Terms**—Array phase error correction, ground-based synthetic aperture radar (GB-SAR), millimeter-wave (mmW) radar, multiple-input–multiple-output (MIMO), super-resolution imaging.

## I. INTRODUCTION

THE ground-based synthetic aperture radar (GB-SAR) is a very powerful tool in mapping and deformation monitoring of landslides, buildings, bridges, and so on, which can work all-weather and all-day in a noncontact manner [1], [2], [3], [4], [5], [6]. In contrast to traditional array radar using the real aperture, GB-SAR exploits the motion of radar platform in a mechanical guide to form a relatively large virtual synthetic aperture, which enables high resolution in the azimuth dimension [7], [8], [9], [10], [11], [12], [13], [14], [15]. Incorporating with transmitting a wideband signal, the

Manuscript received 30 September 2023; revised 21 November 2023 and 22 December 2023; accepted 5 January 2024. This work was supported in part by the National Science Foundation of China (NSFC) under Grant 62071113, in part by the Natural Science Foundation of Jiangsu Province under Grant BK20211559, and in part by the Fundamental Research Funds for the Central Universities under Grant 2242022k60008 and Grant 2242022R40008. (*Corresponding author: Gang Xu*)

The authors are with the State Key Laboratory of Millimeter Waves, School of Information Science and Engineering, Southeast University, Nanjing 210096, China (e-mail: gangxu@seu.edu.cn).

Color versions of one or more figures in this article are available at <https://doi.org/10.1109/TMTT.2024.3352406>.

Digital Object Identifier 10.1109/TMTT.2024.3352406

range high-resolution imaging can also be obtained for the achievement of 2-D imaging. Furthermore, 3-D SAR imaging is also studied to be more suitable in the application of complicated terrains, such as buildings and dams, by dealing with layovers [16], [17], [18]. In fact, the aperture in the vertical dimension is indispensable to realize 3-D imaging, where there are usually two methods to be referred as mechanical scanning and physical array. To balance the scanning period and imaging resolution, it is also suggested to use a 1-D array with 1-D scanning in the perpendicular dimension, known as 3-D array SAR.

With the high-integration development of radio frequency (RF) system and radar chip, the millimeter-wave (mmW) radar has gained more and more attention in popularity, which benefits from the small-size, low-cost, and ultrahigh-resolution imaging performances [19], [20], [21], [22], [23], [24], [25]. In the past decades, the mmW radar has been gradually applied in wide applications, such as automotive driving and security imaging [26], [27], [28], [29], [30], [31]. Meanwhile, the mmW radar can also be used in GB-SAR by replacing the microwave radar sensor, which can effectively reduce both the system complexity and cost. To improve the array resolution in elevation, the multiple-input–multiple-output (MIMO) technology is employed, which uses multiple channels to simultaneously transmit orthogonal signals and multiple receiving channels to simultaneously receive echo data [24], [25]. The mmW MIMO radar can greatly increase the aperture of an equivalent array by reducing the system complexity, i.e., channel number of transceiver. Besides, a strategy of multichip cascading has been proposed to greatly increase the scale of MIMO arrays. However, the elevation resolution is still much lower than those of the range and azimuth dimensions, which is a huge challenge for high-resolution imaging tasks. Typically, the range resolution is at the scale of decimeter and the azimuth resolution is at the scale of milliradian. Take 77-GHz radar as an example, and when the rail length is set to about 1 m, the azimuth resolution is  $\Delta\theta \approx 0.0019$  rad. To achieve the same level resolution in elevation, a size of 1–2-m equivalent MIMO array may be required, which can hardly be satisfied in practice.

In the society of array signal processing, angle super-resolution technologies have been widely studied and many powerful algorithms have been proposed, which can be applied to mmW MIMO radar [32]. In the current research, compressive sensing (CS) is widely utilized for array super-resolution imaging, demonstrating notable performance advantages in

low signal-to-noise ratio (SNR) conditions and with the limitation of a single snapshot. This makes CS particularly suitable for GB-SAR imaging [33], [34], [35], [36]. In practical GB-SAR imaging, the assumption that all scatterers are located on a predesigned grid is hardly tenable. Meanwhile, a design of too dense grids tends to deteriorate the CS-based imaging performance. To overcome the drawback of relying on the discrete dictionary, the off-grid CS using atomic norm minimization (ANM) may be a better choice [35], [36]. To address the aforementioned issues, a novel 3-D GB-SAR imaging and array phase error calibration algorithm is proposed for the mmW MIMO radar in this article. In the systematic and comprehensive design of an array 3-D imaging scheme using GB mmW radar, Doppler-division multiplexing (DDM) MIMO of elevation array is designed and a powerful elevation estimation algorithm is proposed to improve imaging performance collaboratively. The design of DDM MIMO enables channel separation without the need for waveform design, reducing system complexity and simplifying signal processing. In particular, compared to time-division multiplexing (TDM), the advantage of DDM in maintaining channel coherence in 3-D imaging is analyzed and emphasized. Then, the 3-D imaging is realized by 2-D SAR imaging using the backprojection (BP) algorithm and followed by the super-resolution imaging using a novel proposed ANM algorithm. The gridless super-resolution elevation estimation is achieved using ANM, which can enhance imaging performance under limited aperture and avoid basis mismatch of traditional CS method. In addition, array phase error calibration using the minimum entropy method is proposed, which only needs a single calibration in the laboratory environment to compensate for channel errors throughout the entire imaging processing. The effectiveness is verified and imaging performance is evaluated using a Texas Instruments (TI) 77-GHz radar board with a  $4 \times 8$  MIMO array.

The remainder of this article is organized as follows. The concept and system architecture of DDM MIMO-SAR are introduced in Section II. The basic signal model of MIMO-SAR is addressed in Section III. Next, the proposed 3-D imaging algorithm is introduced in Section IV, including 2-D imaging using the BP algorithm and super-resolution array imaging using the proposed ANM algorithm. Besides, a novel algorithm for array phase error calibration using minimum entropy is also proposed. Finally, experimental analysis is carried out in Section V to confirm the effectiveness of the proposed 3-D GB-SAR imaging algorithm.

## II. CONCEPT AND SYSTEM ARCHITECTURE

### A. Imaging Geometry and Data Acquisition

The 3-D imaging geometry of the array GB-SAR is shown in Fig. 1. The mmW array radar is mounted on the rail platform to scan in a straight line along the horizontal direction, where a vertical array perpendicular to the direction of radar motion is used. In this way, a 2-D virtual aperture in space can be formed with the achievement of both azimuth and elevation resolutions. In other words, the system has acquired the ability to measure azimuth and elevation angles. During the

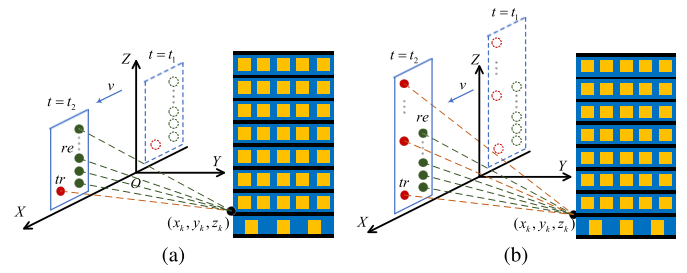


Fig. 1. Imaging geometry of GB. (a) Conventional array SAR. (b) MIMO-SAR.

scanning period, the radar system operates in a strip forward side view to observe interesting scenes, such as buildings and mountain areas. Incorporating with range resolution by transmitting wideband waveform, the GB radar system can obtain the 3-D imaging capability. As shown in Fig. 1, the radar motion direction is set as the X-axis, the radar antenna beam pointing is set as the Y-axis, and the antenna layout direction is set as the Z-axis. The 2-D spatial resolution in the  $XOY$  plane depends on SAR imaging, while the elevation resolution depends on the used array.

For the micro mmW radar, the type of frequency-modulated continuous wave (FMCW) has been widely adopted due to its advantages of large bandwidth and low system complexity. During GB-SAR imaging, a series of chirps are transmitted in a constant period, i.e., pulse repetition frequency (PRF). On the receiver, the dechirp mode is applied by transferring the wideband echo data to small band, where the backscattered signal is demodulated using the referred transmitted signal. In this way, the demodulated signal is reduced to a beat and intermediate frequency, which is proportional to the range of scatterers. Fig. 2 shows the system diagram and the time-frequency diagram of the dechirp processing of FMCW radar. Note that the beat frequency is used to measure the range of targets. Typically, it is generally believed that GB-SAR imaging can be described using a “stop and go” model by neglecting the influence of radar motion during receiving.

### B. Design of DDM MIMO-SAR

Based on the observation that the elevation resolution is significantly lower compared with the range and azimuth dimensions, the MIMO-SAR system has been designed to enhance the elevation resolution and overcome the limitations of array size. In this framework of MIMO radar, some of the multiple channels simultaneously transmit coded orthogonal signals, while the other multiple channels separately receive the backscattered signals. By using waveform orthogonal technology, signals from different transmission channels can be separated at the end of receivers, resulting in a much larger number of equivalent channels to greatly increase the array size. The 3-D imaging geometry of GB MIMO-SAR is shown in Fig. 1(b) and the usage of a transmitter array is a major difference from that of the array SAR shown in Fig. 1(a).

For the MIMO-SAR system, it is necessary to design an appropriate orthogonal waveform to achieve perfect echo separation from different transmitters on one receiver. For

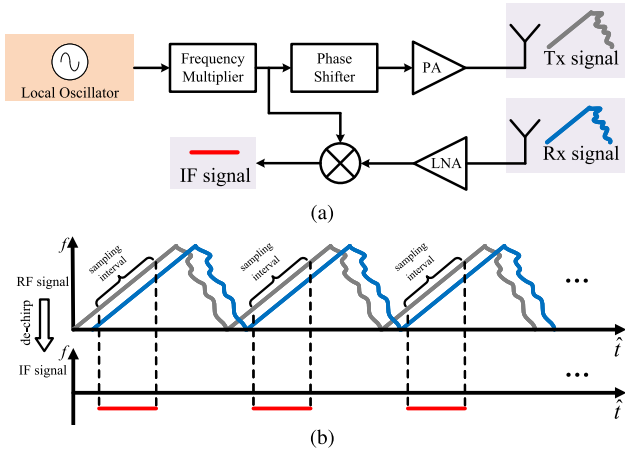


Fig. 2. Diagram of dechirp processing from the perspective of (a) FMCW radar system and (b) time–frequency relationship.

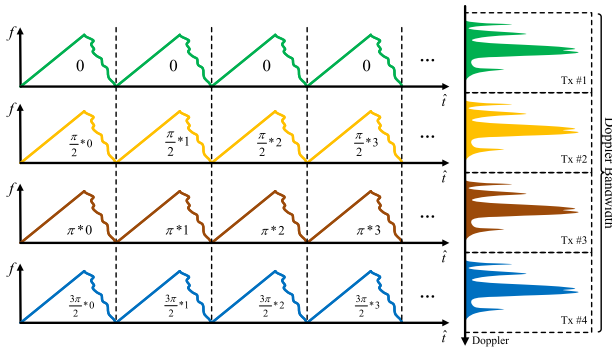


Fig. 3. Typical four-antenna Doppler encoding diagram.

simple implementation, the most common choice is TDM MIMO by switching the working status of transmitters at different times in sequence. The primary advantage of TDM is that no additional multichannel data separation processing is required. However, TDM tends to reduce transmission power by a factor of  $P$ , i.e., the number of transmitters, and it will introduce incoherent artifacts, i.e., phase errors, on the MIMO array due to the movement of radar platform, which is a big challenge for GB-SAR imaging [31].

Taking into account these aforementioned factors, a strategy of DDM MIMO-SAR is employed and each transmitter is coded in pulses using different linear phase sequences. In practice, a specific implementation is to use a multibit phase shifter array connected to each transmitter, which can be integrated into a multiple output mmW radar chip. A typical four-antenna Doppler encoding diagram is shown in Fig. 3. For one receiver, the received signals from the four transmitters are obviously separated in the Doppler domain and four banks of Doppler spectrum filter can be used as the decoder. Compared with TDM mode, the DDM MIMO-SAR obviates the necessity for a complex compensation algorithm and can attain significantly greater transmission power with the cost of additional encoding and channel separation.

### III. SIGNAL MODEL

In this section, the signal model of DDM MIMO-SAR is introduced as the basis of the following 3-D SAR imaging.

Assuming that the radar emits FMCW signals, the signal transmitted by the  $p$ th transmitting antenna can be described as

$$s_t^p(\hat{t}, t_m) = G_p \cdot \text{rect}\left(\frac{\hat{t}}{T}\right) \cdot \exp(j2\pi f_c(\hat{t} + t_m)) \cdot \exp(j\pi\gamma\hat{t}^2) \cdot \exp(j(m-1)\varphi_d^p) \quad (1)$$

where  $\text{rect}(\hat{t}/T) = 1$  for  $0 \leq \hat{t} \leq T$ , otherwise 0. The variables  $m$ ,  $G_p$ ,  $\hat{t}$ ,  $t_m$ ,  $T$ ,  $f_c$ , and  $\gamma$  are the pulse index, gain of the  $p$ th transmitting antenna, fast time, slow time, pulselength, carrier frequency, and chirp rate, respectively. Besides,  $\varphi_d^p$  is the phase stepping value implemented by the phase shifter of the Doppler encoding for the  $p$ th transmitting channel. The propagation distance of the electromagnetic wave transmitted by the  $p$ th transmitting antenna, reflected by the  $k$ th scatterer  $\mu_k$  located at  $(x_k, y_k, z_k)$ , and received by the  $q$ th receiving antenna at time  $t_m$  can be given as

$$R_k^{p,q}(t_m) = \sqrt{(x_k - vt_m)^2 + y_k^2 + (z_k - z_p)^2} + \sqrt{(x_k - vt_m)^2 + y_k^2 + (z_k - z_q)^2} \quad (2)$$

where  $v$  is the velocity of radar platform and  $z_p$  and  $z_q$  denote the elevation coordinate of  $p$ th transmitter and  $q$ th receiver, respectively. Due to the size of MIMO array being much smaller than the distance from the radar to scatterers, the array can generally be considered to meet the far-field condition. Under the far-field condition, the propagation distance  $R_k^{p,q}$  can be approximately expressed as

$$R_k^{p,q}(t_m) \approx 2\sqrt{(x_k - vt_m)^2 + y_k^2 + z_k^2} - (z_p + z_q) \sin \theta_k = 2R_k(t_m) - (z_p + z_q) \sin \theta_k \quad (3)$$

where  $R_k(t_m) = ((x_k - vt_m)^2 + y_k^2 + z_k^2)^{1/2}$  and  $\theta_k = \arcsin(z_k/R_k(t_m))$  is the elevation angle of  $\mu_k$  relative to the radar. The echo signal received by the  $q$ th receiving antenna can be written as

$$\begin{aligned} s_r^q(\hat{t}, t_m) &= G_q \sum_{p=1}^P G_p \sum_{k=1}^K \sigma_k \cdot \text{rect}\left(\frac{\hat{t} - \frac{R_k^{p,q}(t_m)}{c}}{T}\right) \\ &\quad \cdot \exp\left(j2\pi f_c\left(\hat{t} + t_m - \frac{R_k^{p,q}(t_m)}{c}\right)\right) \\ &\quad \cdot \exp\left(j\pi\gamma\left(\hat{t} - \frac{R_k^{p,q}(t_m)}{c}\right)^2\right) \cdot \exp(j(m-1)\varphi_d^p) \end{aligned} \quad (4)$$

where  $G_q$  and  $\sigma_k$  are the gain of the  $q$ th receiving antenna and scattering coefficient of  $p_k$ , respectively, and  $c$  is the light speed. Besides,  $P$  and  $K$  are the total number of transmitters and scatterers, respectively. For FMCW radar, it is customary to perform dechirp operation to convert the signal from the carrier frequency to the intermediate frequency, specifically by mixing the received signal with the transmitted signal. In (4), the residual video phase (RVP) is relatively minor compared to other signal components and can be corrected [37].

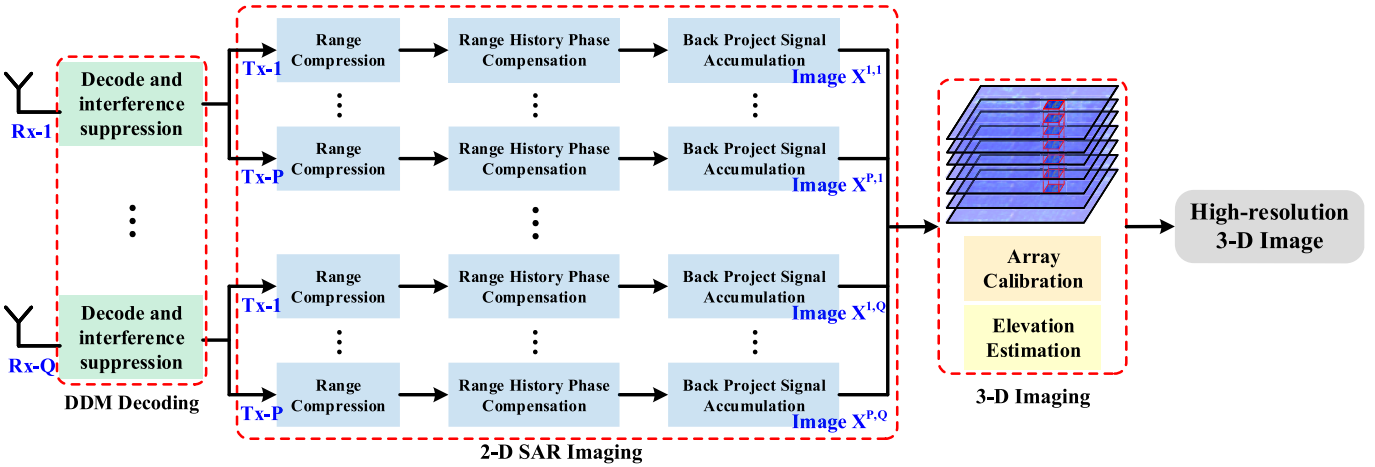


Fig. 4. Signal processing flowchart of 3-D GB-SAR imaging.

After low-pass filter and substituting (3) into (4), the signal could be expressed as

$$\begin{aligned}
 & s_r^q(\hat{t}, t_m) \\
 &= G_q \sum_{p=1}^P G_p \sum_{k=1}^K \sigma_k \cdot \text{rect}\left(\frac{\hat{t} - \frac{R_k^{p,q}(t_m)}{c}}{T}\right) \\
 &\quad \cdot \exp\left(-\frac{j2\pi\gamma R_k^{p,q}(t_m)}{c}\hat{t}\right) \cdot \exp\left(-\frac{j4\pi f_c R_k(t_m)}{c}\right) \\
 &\quad \cdot \exp(j(m-1)\varphi_d^p) \\
 &\approx G_q \sum_{p=1}^P G_p \sum_{k=1}^K \sigma_k \cdot \text{rect}\left(\frac{\hat{t} - \frac{2R_k(t_m)}{c}}{T}\right) \\
 &\quad \cdot \exp\left(-\frac{j4\pi\gamma R_k(t_m)}{c}\hat{t}\right) \cdot \exp\left(-\frac{j4\pi f_c R_k(t_m)}{c}\right) \\
 &\quad \cdot \exp\left(\frac{j2\pi f_c(z_p + z_q)}{c} \sin \theta_k\right) \cdot \exp(j(m-1)\varphi_d^p). \quad (5)
 \end{aligned}$$

The approximation ignored differences of envelope and phase with respect to array element position since the effect caused by array element position on the envelope of range profile is less than 1/4 range cell, without introducing migration through range cell [38].

Before imaging, the signal components from different transmitters at one receiver need to be separated. First, (5) can be represented in a discrete form as

$$\begin{aligned}
 s_r^q(l, m) &= G_q \sum_{p=1}^P G_p \sum_{k=1}^K \sigma_k \cdot \exp\left(-\frac{j4\pi\gamma R_k(m)}{c} \cdot \frac{l-1}{f_s}\right) \\
 &\quad \cdot \exp\left(\frac{j2\pi f_c(z_p + z_q)}{c} \sin \theta_k\right) \\
 &\quad \cdot \exp\left(-\frac{j4\pi f_c R_k(m)}{c}\right) \cdot \exp(j(m-1)\varphi_d^p) \\
 &= \sum_{p=1}^P s_r^{p,q}(l, m) \cdot \exp(j(m-1)\varphi_d^p) \quad (6)
 \end{aligned}$$

where  $l$  and  $f_s$  are in-pulse sample index and sample frequency, respectively, and  $R_k(m)$  represents the range samples in pulses. For DDM MIMO, the discrete Fourier transform (DFT) can be used to separate signals with different Doppler codes in the Doppler spectrum domain as

$$\begin{aligned}
 S_r^q(l, \omega) &= \text{DFT}^m(s_r^q(l, m)) \\
 &= \text{DFT}^m\left(\sum_{p=1}^P s_r^{p,q}(l, m) \cdot \exp(j(m-1)\varphi_d^p)\right) \\
 &= \sum_{p=1}^P \text{DFT}^m(s_r^{p,q}(l, m) \cdot \exp(j(m-1)\varphi_d^p)) \\
 &= \sum_{p=1}^P S_r^{p,q}\left(l, \omega - \frac{\varphi_d^p M}{2\pi}\right) \quad (7)
 \end{aligned}$$

where  $M$  is the number of pulses.  $\text{DFT}^m(\cdot)$  means performing DFT on signals with variable  $m$  and  $(*)$  denotes the convolution operation. Note that the coded signals can be separated in the Doppler spectrum domain and the Doppler center shift is proportional to the value of  $\varphi_d^p$ . The following limitation should be satisfied to avoid Doppler spectrum aliasing:

$$\left| \frac{2v \sin(\theta_{BW}/2)}{\lambda} \right| < \frac{\text{PRF}}{2P} \quad (8)$$

where  $\theta_{BW}$  is the beamwidth of transmitting antenna and  $\lambda$  is the wavelength of radar system. After successful separation in the Doppler spectrum domain, the signals of each virtual channel can be represented as

$$\begin{aligned}
 s^{p,q}(l, m) &= G_p G_q \sum_{k=1}^K \sigma_k \cdot \exp\left(-\frac{j4\pi\gamma R_k(m)}{c} \cdot \frac{l-1}{f_s}\right) \\
 &\quad \cdot \exp\left(\frac{j2\pi f_c(z_p + z_q)}{c} \sin \theta_k\right) \\
 &\quad \cdot \exp\left(-\frac{j4\pi f_c R_k(m)}{c}\right). \quad (9)
 \end{aligned}$$

#### IV. IMAGING ALGORITHM

In this section, the proposed 3-D MIMO-SAR imaging algorithm is introduced in detail based on the signal model in Section II. As shown in Fig. 4, the overall algorithm process can be divided into three main parts. In Section IV-A, the MIMO data are decoded in each receiving channel, followed by the application of the 2-D SAR imaging using the BP approach, which is particularly suitable for near-field imaging applications. In Section IV-B, the proposed off-grid CS algorithm of ANM is applied for the array super-resolution imaging, which aims to effectively overcome the resolution limitation of the MIMO array. In fact, the same pixels from the multichannel 2-D images are stacked and processed using the array signal processing technology to obtain the corresponding elevation information. Section IV-C involves MIMO array phase error correction, which is necessary for accurate array imaging. We employ a minimum entropy algorithm to precisely estimate the array errors utilizing measured data in an active calibration manner.

##### A. 2-D SAR Imaging Using BP Algorithm

The BP algorithm is introduced to ensure the focusing quality, which is the basic precondition of 3-D GB-SAR imaging. The typical procedures of BP include range interpolation, phase compensation, and accumulating multiple pulses. Interpolated fast Fourier transform (FFT) is first performed for range compression and the corresponding range cell is selected for a certain position in the scene. The phase change resulting from platform motion is then compensated to the same platform position. Finally, multiple chirps that have been compensated are used for azimuth coherent accumulation. The range spectrum after pulse compression can be expressed as

$$\begin{aligned} S_r^{p,q}(l', m) &= \alpha L G_p G_q \sum_{k=1}^K \sigma_k \cdot \text{sinc}\left((l' - 1) - \alpha \frac{2B}{c} R_k(m)\right) \\ &\quad \cdot \exp\left(\frac{j2\pi f_c(z_p + z_q)}{c} \sin \theta_k\right) \cdot \exp\left(-\frac{j4\pi f_c R_k(m)}{c}\right) \end{aligned} \quad (10)$$

where  $\alpha$  is the interpolation coefficient [39] and we usually take  $\alpha = 10$ . The variable  $B$  is the signal bandwidth and  $l' = 1, 2, \dots, \alpha L$  is the index of cells in the range spectrum after interpolation. In the process of coherent accumulation, the distance between the scatterer  $\mu$  located at  $(x, r)$  and the radar at the time of each pulse emission can be written as

$$R(m) = \sqrt{\left(x - \frac{v(m-1)}{\text{PRF}}\right)^2 + r^2} \quad (11)$$

where  $r = (y^2 + z^2)^{1/2}$  is the slant range and the corresponding grid index on the range spectrum can be calculated as

$$\text{idx}(m) = \text{round}\left(\frac{2\alpha B}{c} R(m)\right) \quad (12)$$

where  $\text{round}(\cdot)$  denotes rounding the decimal up to the nearest integer. Accumulate all pulses to obtain the final 2-D SAR

image for each channel as follows:

$$X_{2\text{-D}}^{p,q}(x, r) = \sum_{m=1}^M S_r^{p,q}(\text{idx}(m), m) \cdot \exp\left(\frac{j4\pi f_c R_k(m)}{c}\right). \quad (13)$$

##### B. Super-Resolution 3-D Imaging Using ANM

The range resolution can usually reach the centimeter level owing to the large bandwidth provided by the mmW frequency band, but the elevation resolution is often much lower due to array aperture limitation. To further improve the 3-D imaging performance in array resolution, an off-grid CS algorithm of ANM is employed to effectively avoid the discrete error of the Fourier dictionary. Generally, the 3-D imaging is implemented in a “2-D + 1-D” manner [34], i.e., the elevation estimation is performed on each pixel of stacked 2-D images. It is assumed that  $K$  scatterers are located in certain range–azimuth pixel located at  $(x, r)$  and the corresponding signal of all  $N = P \times Q$  channels  $\mathbf{x}$  can be expressed as

$$\mathbf{x} = \sum_{k=1}^K \mathbf{a}(\theta_k) s_k + \mathbf{e} = \mathbf{A}(\boldsymbol{\theta}) \mathbf{s} + \mathbf{e} \quad (14)$$

where  $\mathbf{a}(\theta_k) = [e^{j2\pi z_1 \sin(\theta_k)/\lambda}, \dots, e^{j2\pi z_N \sin(\theta_k)/\lambda}]^T$  is the array guiding vector corresponding to the incident angle  $\theta_k$ ,  $\mathbf{A}(\boldsymbol{\theta}) = [\mathbf{a}(\theta_1), \dots, \mathbf{a}(\theta_K)]$ , and  $\mathbf{s} = [s_1, \dots, s_K]^T$  is the scatter coefficient of each target. The vector  $\mathbf{e}$  represents Gaussian white noise and  $[z_1, \dots, z_N]$  are elevation coordinates of each array element. The array signal  $\mathbf{x}$  can be treated as a combination of atom series with the atomic set  $\mathcal{A}$ , which is defined as

$$\mathcal{A} \triangleq \left\{ \mathbf{a}(\theta_k) | \theta_k \in \left[-\frac{\pi}{2}, \frac{\pi}{2}\right) \right\} \quad (15)$$

and the atomic norm of  $\mathbf{x}$  is defined as

$$\|\mathbf{x}\|_{\mathcal{A}} \triangleq \inf \left\{ \sum_k s_k : \mathbf{x} = \sum_k \mathbf{a}(\theta_k) s_k, s_k \geq 0, \mathbf{a}(\theta_k) \in \mathcal{A} \right\} \quad (16)$$

where  $\inf(\cdot)$  denotes taking the infimum. The atomic soft thresholding (AST) method can be used to eliminate the influence of Gaussian noise and estimate the covariance matrix [36]

$$\min_{\tilde{\mathbf{x}}} \|\tilde{\mathbf{x}}\|_{\mathcal{A}} \quad \text{s.t. } \|\tilde{\mathbf{x}} - \mathbf{x}\|_2^2 \leq \sigma \quad (17)$$

where  $\tilde{\mathbf{x}}$  is the measurement and  $\sigma$  is the noise variance of  $\mathbf{e}$ . The atomic norm  $\|\tilde{\mathbf{x}}\|_{\mathcal{A}}$  can be solved via semidefinite programming as

$$\|\tilde{\mathbf{x}}\|_{\mathcal{A}} = \min_{\rho, \mathbf{u}} \frac{1}{2} (\rho + u_1) \quad \text{s.t. } \begin{bmatrix} \rho & \tilde{\mathbf{x}}^H \\ \tilde{\mathbf{x}} & T(\mathbf{u}) \end{bmatrix} \succeq \mathbf{0} \quad (18)$$

where  $\mathbf{u}$  is an  $M \times 1$  vector and  $T(\mathbf{u})$  is a Toeplitz matrix generated by  $\mathbf{u}$ . Besides,  $\rho$  and  $u_1$  are the variables to be optimized and the principal diagonal element of  $T(\mathbf{u})$ , respectively.  $(\cdot)^H$  denotes the Hermitian operation, and  $\mathbf{A} \succeq \mathbf{0}$  means that  $\mathbf{A}$  is a positive semidefinite matrix. Therefore, (17) could be written as

$$\min_{\rho, \mathbf{u}, \tilde{\mathbf{x}}} \frac{\mu}{2} (\rho + u_1) + \frac{1}{2} \|\tilde{\mathbf{x}} - \mathbf{x}\|_2^2 \quad \text{s.t. } \begin{bmatrix} \rho & \tilde{\mathbf{x}}^H \\ \tilde{\mathbf{x}} & T(\mathbf{u}) \end{bmatrix} \succeq \mathbf{0} \quad (19)$$

where  $T(\mathbf{u})$  is the denoising estimate of the covariance matrix of the array. Taking  $T(\mathbf{u})$  as the covariance matrix, we can obtain  $\mathbf{A}(\theta)$  via the Root MUSIC algorithm and achieve super-resolution 3-D imaging.

### C. Array Phase Error Calibration Using Minimum Entropy Method

For MIMO mmW radar, channel errors are usually unavoidable. The current mmW radar system often relies on multichip cascades to achieve multiple transmitting and receiving channels. Although the multiple chips share a local oscillator to keep the consistency of signals between channels, the phase errors within and between chips are still non-ignorable. In this case, the presence of array phase errors tends to introduce some artifacts, including widening or splitting of the main lobe, rising of the sidelobe, and shifting of peak position. In the following, a minimum entropy algorithm [40] is used to deal with the array phase errors in an active calibration manner.

The echo data are collected using the corner reflectors placed at different elevation angles, i.e., multiple experiments. Assuming that a stationary point target is used as a calibration for error correction, the signals of each channel with a target placed at different elevation angles  $\theta_i$  can be written as

$$x_{i,n} = |x_{i,n}| \exp\left(j\left(\frac{2\pi z_n \sin \theta_i}{\lambda} + \psi_0(i) + \gamma(n) + e_n(i)\right)\right) \quad (20)$$

where  $x_{i,n}$  is the signal of the  $n$ th channel in the  $i$ th angle measurement result.  $\psi_0(i)$  is the initial phase of the  $i$ th measurement, usually selected as the phase of the first array element.  $\gamma(n)$  is the phase error of elements that needed to be compensated and it is only related to antenna array elements.  $e_n(i)$  is the interference phase noise during measurement.

Performing inverse FFT (IFFT) on the channel dimension of  $x_{i,n}$ , we can obtain

$$z_{i,h} = \frac{1}{N} \sum_{n=1}^N e^{j2\pi(h-1)(n-1)/N} x_{i,n} \quad (21)$$

where  $h = 1, \dots, N$  is the elevation angular frequency index. In the presence of phase errors, assume that  $\boldsymbol{\phi} = [\phi_1, \dots, \phi_N]^T$  represent the phase error that needs to be corrected, and (21) can be rewritten as

$$z_{i,h}(\boldsymbol{\phi}) = \frac{1}{N} \sum_{n=1}^N e^{j2\pi(h-1)(n-1)/N} e^{j\phi_n} x_{i,n}. \quad (22)$$

The phase error is considered to be well-compensated when  $\phi_n = -\gamma(n)$ . To solve this problem, a minimum entropy autofocus algorithm is performed to estimate the phase error  $\gamma(n)$ . For simplicity, we denote  $z_{i,h} = z_{i,h}(\boldsymbol{\phi})$  and assume that

$$E_z = \sum_{i=1}^I \sum_{h=1}^N |z_{i,h}|^2 \quad (23)$$

is the total energy of the image and the total number of measurements is  $I$ . According to Parseval's theorem, note that the total energy  $E_z$  of the image remains unchanged regardless

of the phase errors. If  $p_{i,h} = |z_{i,h}|^2/E_z$  is the energy density of pixel  $p_{i,h}$ , the image entropy can be expressed as

$$\begin{aligned} H(\boldsymbol{\phi}) &= - \sum_{i=1}^I \sum_{h=1}^N p_{i,h} \ln p_{i,h} \\ &= - \frac{1}{E_z} \sum_{i=1}^I \sum_{h=1}^N |z_{i,h}|^2 \ln |z_{i,h}|^2 + \ln E_z. \end{aligned} \quad (24)$$

Based on the criterion that the well-focused image without phase errors has the minimum entropy, the phase error is estimated as

$$\hat{\boldsymbol{\phi}} = \arg \min_{\boldsymbol{\phi}} H(\boldsymbol{\phi}) \quad (25)$$

which can be solved iteratively using the optimization transfer method [40]

$$\phi_n^{(b+1)} = \phi_n^{(b)} + \tan^{-1}(B_n/A_n) \quad (26)$$

where

$$\begin{aligned} B_n &= \frac{2}{NE_z} \operatorname{Im} \left\{ \sum_i \tilde{x}_{i,n} \sum_h e^{j2\pi(h-1)(n-1)/N} z_{i,h}^* \ln |z_{i,h}^{(b)}|^2 \right\} \\ A_n &= \frac{2}{NE_z} \operatorname{Re} \left\{ \sum_i \tilde{x}_{i,n} \sum_h e^{j2\pi(h-1)(n-1)/N} z_{i,h}^* \ln |z_{i,h}^{(b)}|^2 \right\} \\ &\quad - \frac{2}{N^2 E_z} \sum_i |\tilde{x}_{i,n}|^2 \sum_h \ln |z_{i,h}^{(b)}|^2 \end{aligned} \quad (27)$$

where  $\tilde{x}_{i,n} = e^{j\phi_n^{(b)}} x_{i,n}$  represents the phase-corrected signal using the  $b$ th iterative estimation  $\boldsymbol{\phi}^{(b)}$  and  $(\cdot)^*$  is the conjugate operation. The iteration stop criterion can be determined as

$$|H(\boldsymbol{\phi}^{(b+1)}) - H(\boldsymbol{\phi}^{(b)})| < \varepsilon_0 \quad (28)$$

where  $\varepsilon_0$  is a preset threshold and we take  $\varepsilon_0 = 1 \times 10^{-3}$ .

## V. EXPERIMENTAL ANALYSIS

In this section, simulated and measured data experiments are carried out to evaluate the performance of 3-D GB-SAR imaging. A TI 77-GHz radar board as shown in Fig. 5 is used, which consists of a four-chip cascaded array. Four transmitting and eight receiving channels are enabled, which are marked in red. In this way, it is equivalent to a 32-element uniform linear array with half-wavelength spacing. The horizontal field of view of the radar board is about  $\pm 60^\circ$  and the elevation field of view is about  $\pm 15^\circ$ . The DDM MIMO is implemented by controlling a 6-bit phase shifter on transmitters. Taking four pulses as an example, the coded signals corresponding to Fig. 3 are listed in Table I.

The optical image of the designed DDM MIMO GB-SAR system is shown in Fig. 6. In the GB-SAR system, an electric slide rail is used and controlled to move by a mobile Bluetooth, which can achieve a maximum aperture of 1 m. The radar board is connected to the PC through Ethernet to achieve waveform configuration and data transmission. Radar echo data are first stored on the solid-state drive (SSD) included in the radar board and then transmitted to the PC through an Ethernet port for signal processing. The radar board is

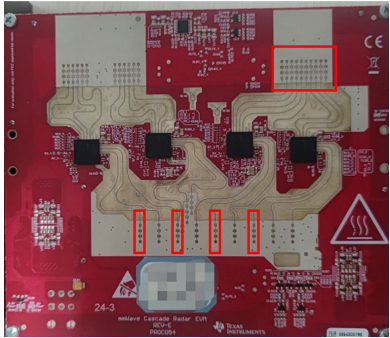


Fig. 5. RF system board of TI AWR2243.

TABLE I  
CODING FOR PHASE SHIFTER OF EACH TRANSMITTER

	Pulse 1	Pulse 2	Pulse 3	Pulse 4
Tx1	“000000”	“000000”	“000000”	“000000”
Tx2	“000000”	“110000”	“100000”	“010000”
Tx3	“000000”	“100000”	“000000”	“100000”
Tx4	“000000”	“010000”	“100000”	“110000”

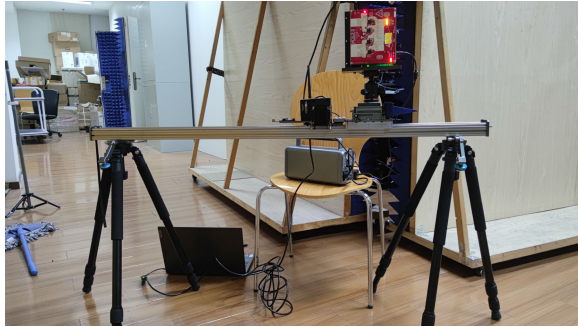


Fig. 6. Optical image of DDM MIMO GB-SAR system.

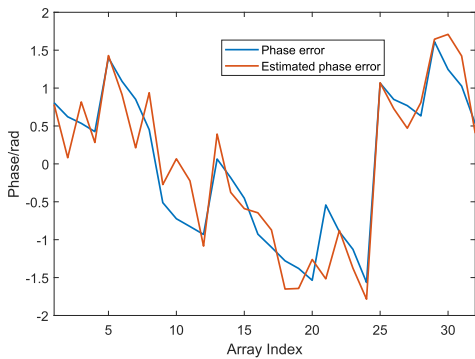


Fig. 7. Exact phase error and estimated phase error of each channel.

fixed on the moving platform of the slide rail using structural components, with the radar parallel to the direction of the slide rail movement and in the forward side view mode.

#### A. Simulation Using Point Targets

Simulation experiments using point targets are carried out to verify the effectiveness of the proposed imaging and array

TABLE II  
LEVATION FREQUENCY ESTIMATION RESULTS OF POINT TARGETS USING DIFFERENT ALGORITHMS

Real location	Before calibration		After calibration	
	$\ell_1$ -NM	ANM	$\ell_1$ -NM	ANM
0.2182	0.1339	0.1321	0.2126	0.2085
0.4472	0.4488	0.4419	0.4331	0.4387
0.2425	0.2441	0.2398	0.2441	0.2442
0.6000	-0.1496	0.5205	0.5906	0.5969
0.1644	0.0866	0.1563	0.1654	0.1626
0.2182	0.1339	0.1348	0.2126	0.2092

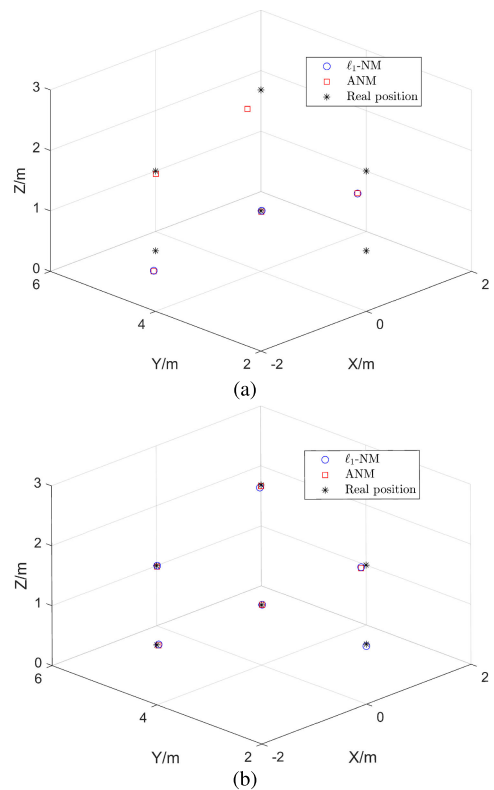


Fig. 8. 3-D SAR images of point targets. (a) Before calibration. (b) After calibration.

calibration algorithm. A 32-element uniform linear array with half-wavelength spacing is simulated to match the equivalent array of the radar board. Six point targets are placed in the scene. The normalized elevation frequencies of each target are listed in the first column of Table II. Gaussian white noise with an SNR of 0 dB is added. In addition, phase error is added on each channel. The value of phase error is shown as a blue curve in Fig. 7, which is set to be the same as the estimated phase error in measured experiments. Meanwhile, the estimated phase error is shown as an orange curve. The 3-D SAR images using the proposed algorithm and the  $\ell_1$  norm minimization ( $\ell_1$ -NM) algorithm [41] before and after array calibration are shown in Fig. 8(a) and (b), respectively. For clarity, the real positions of each point target are marked using black asterisks. The elevation frequency estimation results of each point target are listed in the right columns of Table II.

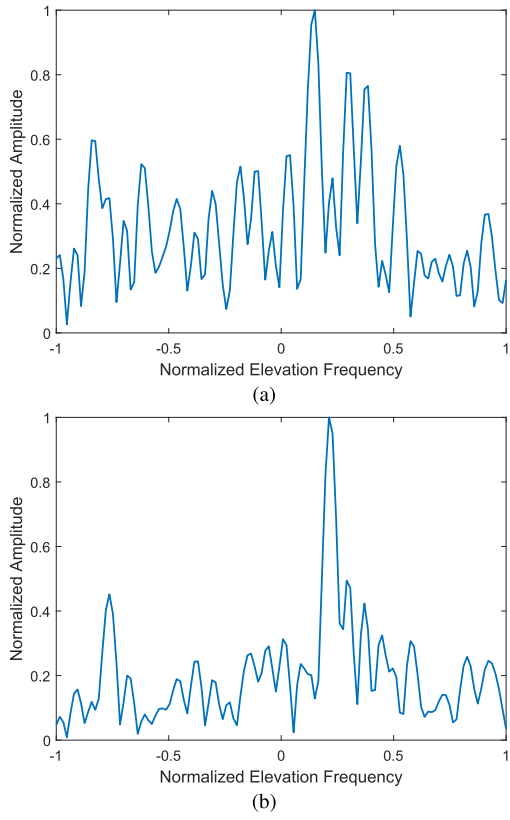


Fig. 9. Elevation spectrum estimation result of P1 before and after array calibration. (a) Before calibration. (b) After calibration.

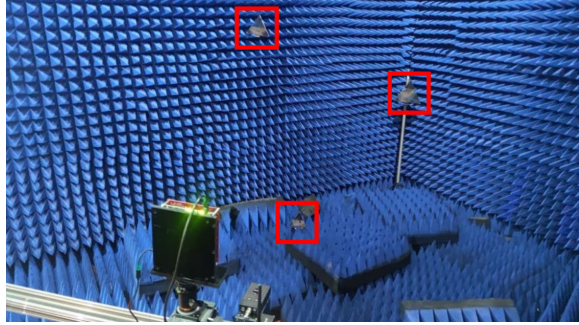


Fig. 10. Imaging scene of corner reflectors.

The elevation spectrum estimation results of the first point target (P1) before and after calibration are shown in Fig. 9(a) and (b), respectively. As shown in Figs. 8 and 9, the elevation estimation results have been effectively improved, and thus, a more accurate 3-D image can be achieved after array calibration.

To quantitatively show the performance of the proposed algorithm and the  $\ell_1$ -NM algorithm, 200 Monte Carlo experiments are conducted. Root-mean-square error (RMSE) of each point target is listed in Table III. It can be seen that the RMSE of both  $\ell_1$ -NM and ANM algorithms are reduced significantly after calibration, which proves the effectiveness of the proposed array calibration algorithm.

#### B. Imaging Analysis Using Corner Reflector Targets

The corner reflectors are placed in the anechoic chamber to evaluate the imaging performance of the point spread

TABLE III  
RMSE OF NORMALIZED ELEVATION FREQUENCY ESTIMATION  
BEFORE AND AFTER ARRAY CALIBRATION

Before calibration		After calibration	
$\ell_1$ -NM	ANM	$\ell_1$ -NM	ANM
0.1343	0.0452	0.0209	0.0210
0.1602	0.0561	0.1036	0.0233
0.0965	0.0633	0.0648	0.0216
0.1812	0.0404	0.0215	0.0207
0.0985	0.0574	0.0291	0.0215
0.1703	0.0451	0.0601	0.0215

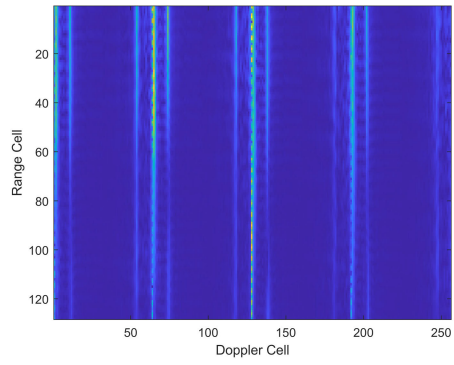


Fig. 11. Doppler spectrum of echo data (receiving channel one).

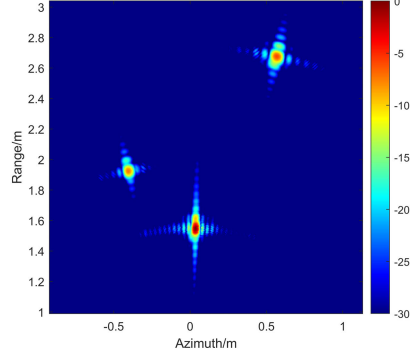


Fig. 12. 2-D SAR image of corner reflectors (receiving channel one).

function. The optical image of imaging scene is shown in Fig. 10. There are three corner reflectors placed at different positions in the anechoic chamber and the corner reflectors are between 1.5- and 3-m distance away from radar. In addition, the key parameters of the DDM MIMO-SAR imaging system are shown in Table IV and the Doppler codes of the four transmitters are

$$\begin{cases} \varphi_d^1 = 0, 0, 0, \dots, 0, \dots, 0 \\ \varphi_d^2 = \frac{\pi}{2}, \pi, \frac{3\pi}{2}, \dots, m\frac{\pi}{2}, \dots, M\frac{\pi}{2} \\ \varphi_d^3 = \pi, 0, \pi, \dots, m\pi, \dots, M\pi \\ \varphi_d^4 = \frac{3\pi}{2}, -\pi, \frac{\pi}{2}, \dots, m\frac{3\pi}{2}, \dots, M\frac{3\pi}{2}. \end{cases} \quad (29)$$

Taking the echo data of the first reflector  $s_r^1(l, m)$  as an example, the azimuth FFT is applied on each receiver transfer to the Doppler domain and its spectrum is shown in Fig. 11. It can be seen that the whole Doppler spectrum is divided into

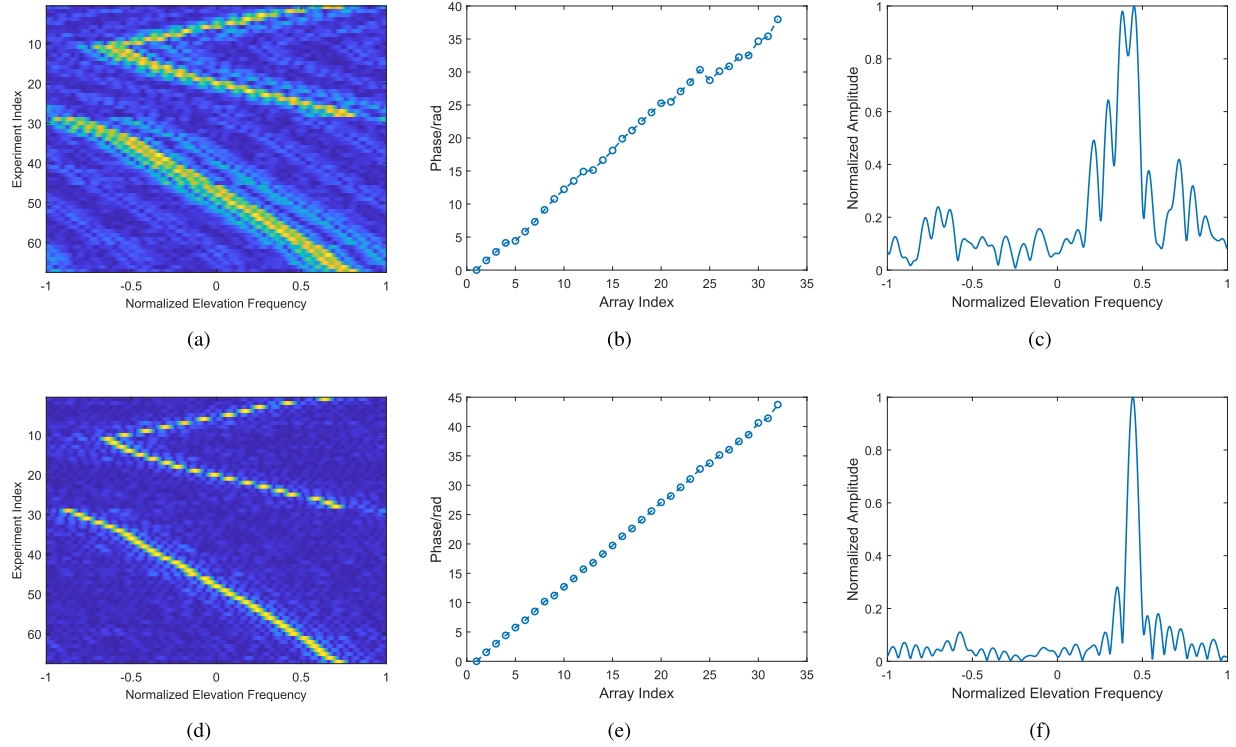


Fig. 13. Comparisons before and after phase error calibration [(a)–(c) before calibration and (d)–(f) after calibration]. (a) and (d) Normalized elevation spectrum of multiple measurements. (b) and (e) Phase curve of 32 channels. (c) and (f) Normalized elevation spectrum of a certain experiment.

TABLE IV  
SYSTEM PARAMETERS OF DDM  
MIMO-SAR IN THE ANECHOIC CHAMBER

System Parameters	Variables	Value
Carrier frequency	$f_c$	77GHz
Bandwidth	$B$	3GHz
Sampling rate	$f_s$	3000kHz
Pulse sampling points	$L$	128
Range resolution	$\Delta R$	0.05m
Utmost unambiguous distance	$R_{max}$	6.4m
Pulse repetition frequency	$PRF$	25Hz
Number of pulses	$M$	64
Coherent pulse interval	$CPI$	2.56s
Velocity of radar	$v$	3.75cm/s
Azimuth resolution	$\Delta A$	$\approx 0.045m$

TABLE V  
SYSTEM PARAMETERS OF DDM MIMO-SAR FOR BUILDING

System Parameters	Variables	Value
Carrier frequency	$f_c$	77GHz
Bandwidth	$B$	1.5GHz
Sampling rate	$f_s$	3000kHz
Pulse sampling points	$L$	512
Range resolution	$\Delta R$	0.1m
Utmost unambiguous distance	$R_{max}$	51.2m
Pulse repetition frequency	$PRF$	33.4Hz
Number of pulses in one channel	$M$	512
Coherent pulse interval	$CPI$	15.33s
Velocity of radar	$v$	3.75cm/s
Azimuth resolution	$\Delta A$	$\approx 0.068m$

four parts and each part corresponds to the signal from the four transmitters. There is no overlapping between each spectrum component. After the successful separation of MIMO signals, BP imaging is performed to generate stacked 2-D images and the incoherent superposition result is shown in Fig. 12. Corresponding to three corner reflectors, three obvious targets can be seen in Fig. 12 and their position matches the actual spatial distribution.

### C. Phase Error Calibration Using Corner Reflector Targets

Next, the effectiveness of the proposed array phase error calibration algorithm of minimum entropy method is verified using the corner reflector target. Place a corner reflector at different positions to obtain the measured data and it has been

repeated 67 times, corresponding to the vertical coordinate of Fig. 13(a) and (d). The image without phase error correction is shown in Fig. 13(a), where the horizontal coordinate represents the normalized elevation frequency estimation. It can be found that the focusing response of each target is very poor due to the presence of phase errors. Then, the phase errors are corrected using the proposed minimum entropy algorithm and the obtained image is shown in Fig. 13(d). Compared with Fig. 13(a), the quality of focus is significantly improved. For a certain measurement, the unwrapped phase curve of 32 MIMO channels of the corner reflector and the corresponding normalized angle spectrum before and after phase error calibration are shown in Fig. 13(b), (c), (e), and (f). It can be seen that before phase error calibration, the phase changes are relatively

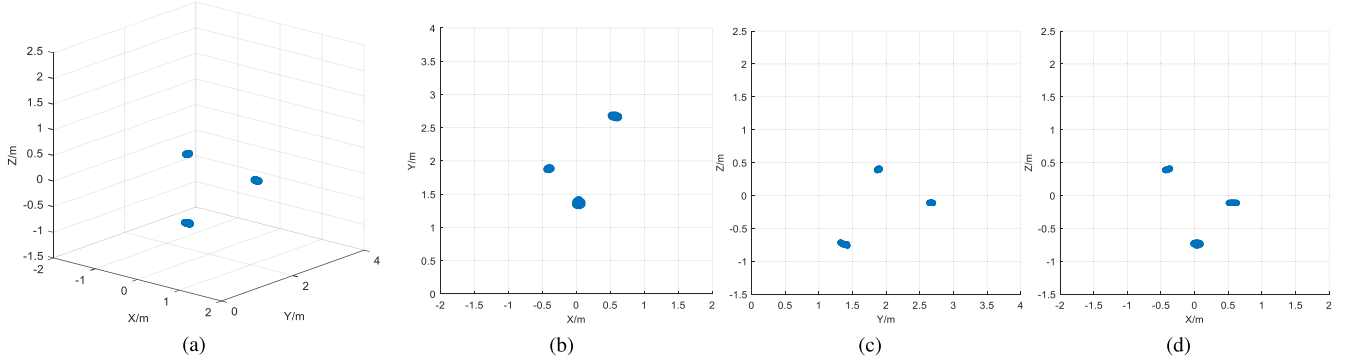


Fig. 14. 3-D SAR images of corner reflectors. (a) Side view. (b) Top view. (c) Right view. (d) Front view.

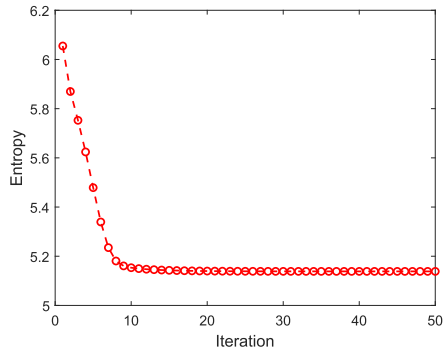


Fig. 15. Entropy of elevation spectrum versus iteration.



Fig. 16. Optical image of the building in measured experiments.

chaotic and the linearity is not good. There are high-level sidelobes to influence the imaging quality significantly. After phase error calibration, the phase curve is almost linear and the pulse response is ideal. The 3-D imaging results after error calibration are shown in Fig. 14 and it is obvious that the three corner reflectors are well-focused and located. The iterative process of image entropy values is shown in Fig. 15, which indicates the fast convergence of the proposed phase error calibration algorithm.

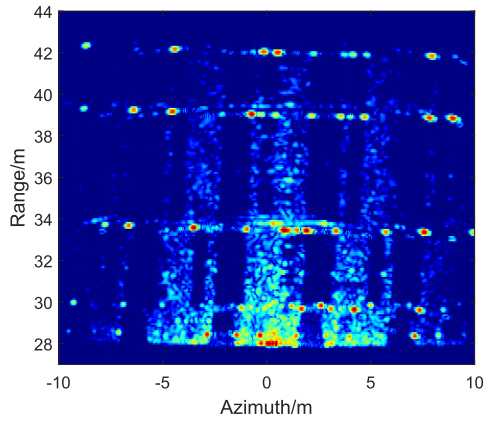


Fig. 17. 2-D SAR image of building (receiving channel one).

TABLE VI  
IMAGE ENTROPY AFTER DENSE PROJECTION

Algorithms	Image Entropy
The proposed algorithm	0.1433
$\ell_1$ -NM algorithm	0.1464

#### D. Imaging Analysis Using Measured Data of Building

In this section, we perform 3-D SAR imaging using the measured data of one building. The key parameters of the DDM MIMO-SAR imaging system for building imaging are shown in Table V. The optical image of the building is shown in Fig. 16, and there are multiple regular square blocks on the surface. Taking a certain channel as an example, Fig. 17 exhibits the 2-D SAR image using the BP algorithm, where the square blocks on the building surface can be clearly distinguished.

Both the ANM and  $\ell_1$ -NM algorithms are applied and the corresponding 3-D imaging results are shown in Figs. 18 and 19, respectively. The colors of point cloud are the mapping of building height. Both point clouds can obviously show the regular contours of the building, but the results shown in Fig. 18 can reflect the structure of the building better by avoiding the problem of discrete position, which verifies the effectiveness and advantage of the proposed algorithm.

To quantitatively assess the quality of the point cloud image without reference imaging results, dense projection of point

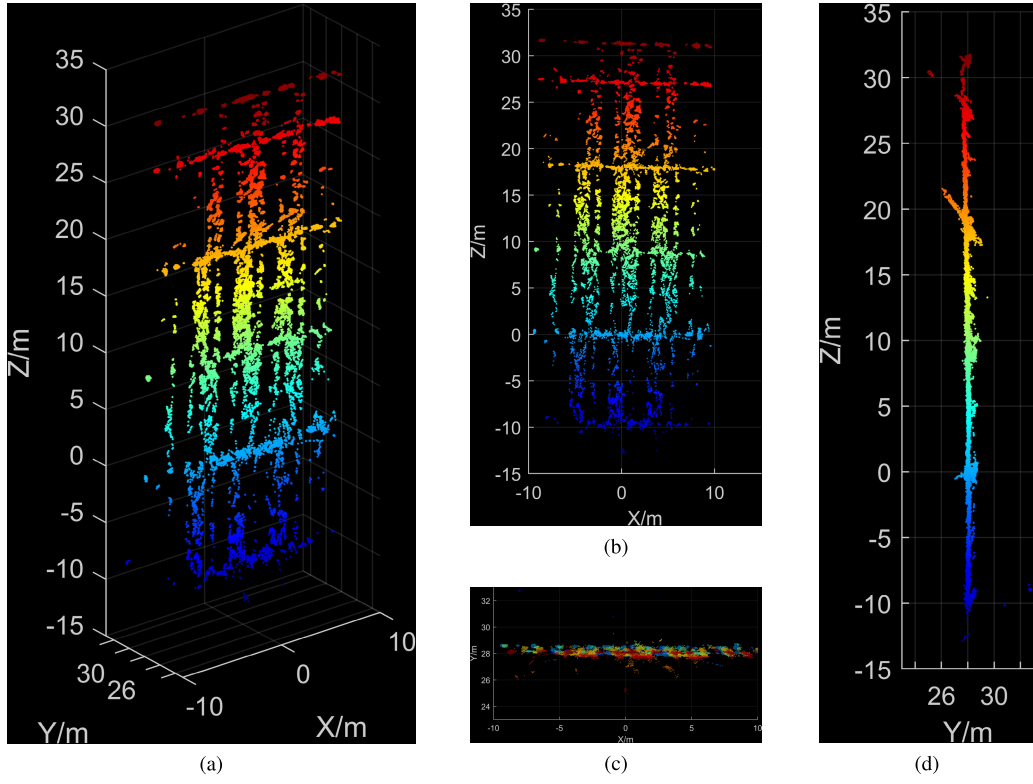


Fig. 18. 3-D SAR images of the proposed algorithm. (a) Side view. (b) Front view. (c) Top view. (d) Right view.

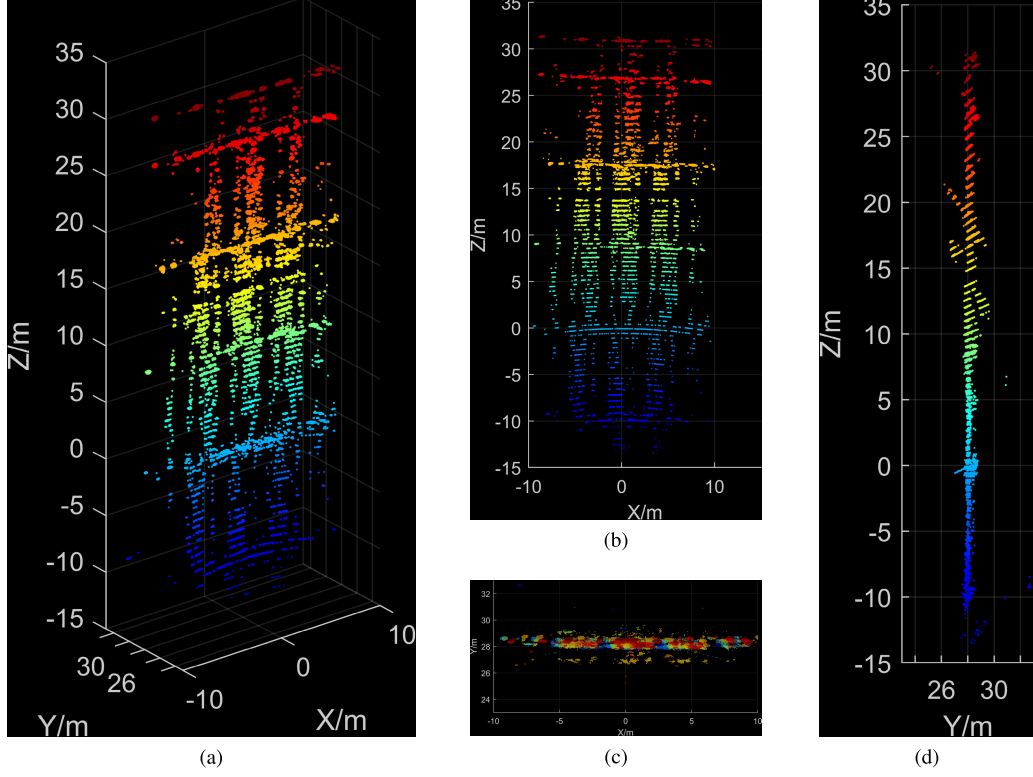


Fig. 19. 3-D SAR images of  $\ell_1$ -NM algorithm. (a) Side view. (b) Front view. (c) Top view. (d) Right view.

cloud to the  $XOY$  plane is performed, as shown in Fig. 20. The comparison of image entropy can reveal the performance of point cloud imaging qualitatively.

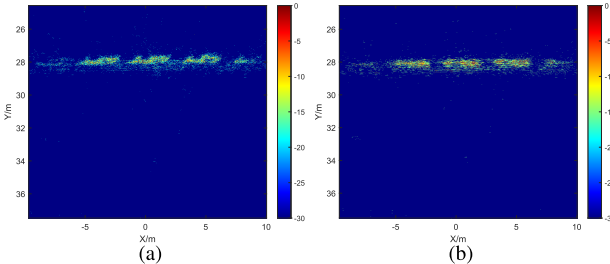


Fig. 20. 2-D images after dense projection. (a) Proposed algorithm. (b)  $\ell_1$ -NM algorithm.

## VI. CONCLUSION

In this article, a 3-D high-resolution SAR imaging and array calibration algorithm is proposed using a GB mmW radar. A framework of DDM MIMO-SAR imaging is designed, which is more suitable for the GB moving platform. The 2-D BP algorithm and a super-resolution elevation estimation algorithm using ANM are proposed for 3-D imaging. In addition, a minimum entropy algorithm is proposed to accurately estimate and correct array phase errors. Experiments in an anechoic chamber and outdoor building observation are carried out using a 77-GHz radar evaluation module with a  $4 \times 8$  MIMO array. In order to pursue imaging quality, the proposed framework has a large calculation consumption, but it can be easily accelerated using parallel computing technology. Our future work will mainly focus on typical applications based on this system, such as deformation monitoring.

## REFERENCES

- [1] S. Wang, W. Feng, K. Kikuta, and M. Sato, "A monostatic/bistatic ground-based synthetic aperture radar system for target imaging and 2-D displacement estimation," *IEEE Geosci. Remote Sens. Lett.*, vol. 18, no. 2, pp. 326–330, Feb. 2021, doi: [10.1109/LGRS.2020.2971662](#).
- [2] X. Zhao, H. Lan, L. Li, Y. Zhang, and C. Zhou, "A multiple-regression model considering deformation information for atmospheric phase screen compensation in ground-based SAR," *IEEE Trans. Geosci. Remote Sens.*, vol. 58, no. 2, pp. 777–789, Feb. 2020, doi: [10.1109/TGRS.2019.2940463](#).
- [3] E. Giusti, S. Gelli, and M. Martorella, "A parametric-model-based approach for atmospheric phase screen removal in ground-based interferometric SAR," *IEEE J. Sel. Topics Appl. Earth Observ. Remote Sens.*, vol. 15, pp. 889–900, 2022, doi: [10.1109/JSTARS.2021.3136940](#).
- [4] M. Pieraccini and L. Miccinesi, "ArcSAR: Theory, simulations, and experimental verification," *IEEE Trans. Microw. Theory Techn.*, vol. 65, no. 1, pp. 293–301, Jan. 2017, doi: [10.1109/TMTT.2016.2613926](#).
- [5] M. García-Fernández, G. Álvarez-Narciso, Y. Álvarez López, and F. Las-Heras, "Array-based ground penetrating synthetic aperture radar on board an unmanned aerial vehicle for enhanced buried threats detection," *IEEE Trans. Geosci. Remote Sens.*, vol. 61, 2023, Art. no. 5104218, doi: [10.1109/TGRS.2023.3272982](#).
- [6] F. Falabella, A. Perrone, T. A. Stabile, and A. Pepe, "Atmospheric phase screen compensation on wrapped ground-based SAR interferograms," *IEEE Trans. Geosci. Remote Sens.*, vol. 60, 2022, Art. no. 5202115, doi: [10.1109/TGRS.2021.3055648](#).
- [7] H. Chai, X. Lv, and P. Xiao, "Deformation monitoring using ground-based differential SAR tomography," *IEEE Geosci. Remote Sens. Lett.*, vol. 17, no. 6, pp. 993–997, Jun. 2020, doi: [10.1109/LGRS.2019.2938233](#).
- [8] Z.-S. Zhou, W.-M. Boerner, and M. Sato, "Development of a ground-based polarimetric broadband SAR system for noninvasive ground-truth validation in vegetation monitoring," *IEEE Trans. Geosci. Remote Sens.*, vol. 42, no. 9, pp. 1803–1810, Sep. 2004, doi: [10.1109/TGRS.2004.832248](#).
- [9] R. Iglesias et al., "Ground-based polarimetric SAR interferometry for the monitoring of terrain displacement phenomena—Part I: Theoretical description," *IEEE J. Sel. Topics Appl. Earth Observ. Remote Sens.*, vol. 8, no. 3, pp. 980–993, Mar. 2015, doi: [10.1109/JSTARS.2014.2360040](#).
- [10] R. Iglesias et al., "Ground-based polarimetric SAR interferometry for the monitoring of terrain displacement phenomena—Part II: Applications," *IEEE J. Sel. Topics Appl. Earth Observ. Remote Sens.*, vol. 8, no. 3, pp. 994–1007, Mar. 2015, doi: [10.1109/JSTARS.2014.2366711](#).
- [11] T. Zeng, C. Mao, C. Hu, and W. Tian, "Ground-based SAR wide view angle full-field imaging algorithm based on keystone formatting," *IEEE J. Sel. Topics Appl. Earth Observ. Remote Sens.*, vol. 9, no. 6, pp. 2160–2170, Jun. 2016, doi: [10.1109/JSTARS.2016.2558578](#).
- [12] Y. Wang, Q. Zhang, Y. Lin, Z. Zhao, and Y. Li, "Multi-phase-center sidelobe suppression method for circular GBSAR based on sparse spectrum," *IEEE Access*, vol. 8, pp. 133802–133816, 2020, doi: [10.1109/ACCESS.2020.3010584](#).
- [13] Y. Zhou et al., "SAR ground moving target refocusing by combining mRe<sup>3</sup> network and TVB-LSTM," *IEEE Trans. Geosci. Remote Sens.*, vol. 60, 2022, Art. no. 5200814, doi: [10.1109/TGRS.2020.3033656](#).
- [14] Y. Izumi, G. Nico, and M. Sato, "Time-series clustering methodology for estimating atmospheric phase screen in ground-based InSAR data," *IEEE Trans. Geosci. Remote Sens.*, vol. 60, 2022, Art. no. 5206309, doi: [10.1109/TGRS.2021.3072037](#).
- [15] T. G. Yitayew, L. Ferro-Famil, T. Eltoft, and S. Tebaldini, "Tomographic imaging of Fjord ice using a very high resolution ground-based SAR system," *IEEE Trans. Geosci. Remote Sens.*, vol. 55, no. 2, pp. 698–714, Feb. 2017, doi: [10.1109/TGRS.2016.2613900](#).
- [16] Z. Huang, J. Sun, W. Tan, P. Huang, and Y. Qi, "A fast far-field pseudopolar format algorithm for ground-based arc 3-D SAR imaging," *IEEE Geosci. Remote Sens. Lett.*, vol. 17, no. 10, pp. 1697–1701, Oct. 2020, doi: [10.1109/LGRS.2019.2952164](#).
- [17] D. Reale, F. Serafino, and V. Pascazio, "An accurate strategy for 3-D ground-based SAR imaging," *IEEE Geosci. Remote Sens. Lett.*, vol. 6, no. 4, pp. 681–685, Oct. 2009, doi: [10.1109/LGRS.2009.2023537](#).
- [18] W. Tian, W. Yang, T. Dang, Z. Zhao, and X. Han, "Three-dimensional ground-based SAR imaging algorithm based on keystone formatting and subblock," *IEEE Access*, vol. 8, pp. 90118–90131, 2020, doi: [10.1109/ACCESS.2020.2993812](#).
- [19] R. Zhou, "A compact MIMO automotive radar using phase-aligned daisy-chain cascading topology and elevation compensation for 2D angle estimation," *Sci. China Inf. Sci.*, vol. 66, Sep. 2023, Art. no. 162305, doi: [10.1007/s11432-022-3613-6](#).
- [20] M. Steiner, T. Grebner, and C. Waldschmidt, "Millimeter-wave SAR-imaging with radar networks based on radar self-localization," *IEEE Trans. Microw. Theory Techn.*, vol. 68, no. 11, pp. 4652–4661, Nov. 2020, doi: [10.1109/TMTT.2020.2995225](#).
- [21] A. Frischen, J. Hasch, and C. Waldschmidt, "A cooperative MIMO radar network using highly integrated FMCW radar sensors," *IEEE Trans. Microw. Theory Techn.*, vol. 65, no. 4, pp. 1355–1366, Apr. 2017, doi: [10.1109/TMTT.2016.2647701](#).
- [22] M. Pauli et al., "Miniaturized millimeter-wave radar sensor for high-accuracy applications," *IEEE Trans. Microw. Theory Techn.*, vol. 65, no. 5, pp. 1707–1715, May 2017, doi: [10.1109/TMTT.2017.2677910](#).
- [23] D. Ma et al., "Millimeter-wave 3-D imaging using leaky-wave antennas and an extended Rytov approximation in a frequency-diverse MIMO system," *IEEE Trans. Microw. Theory Techn.*, vol. 71, no. 4, pp. 1809–1825, Apr. 2023, doi: [10.1109/TMTT.2022.3223931](#).
- [24] T. Kitamura and K. Suwa, "Doppler division multiplexed multiple-input–multiple-output imaging using cascaded millimeter-wave radars," *IEEE Trans. Microw. Theory Techn.*, vol. 70, no. 3, pp. 1571–1581, Mar. 2022, doi: [10.1109/TMTT.2021.3123129](#).
- [25] M. Q. Nguyen, R. Feger, J. Bechter, M. Pichler-Scheder, M. H. Hahn, and A. Stelzer, "Fast-chirp FDMA MIMO radar system using range-division multiple-access and Doppler-division multiple-access," *IEEE Trans. Microw. Theory Techn.*, vol. 69, no. 1, pp. 1136–1148, Jan. 2021, doi: [10.1109/TMTT.2020.3039795](#).
- [26] S.-Y. Jeon et al., "W-band MIMO FMCW radar system with simultaneous transmission of orthogonal waveforms for high-resolution imaging," *IEEE Trans. Microw. Theory Techn.*, vol. 66, no. 11, pp. 5051–5064, Nov. 2018, doi: [10.1109/TMTT.2018.2867003](#).
- [27] D. Blehn et al., "W-band time-domain multiplexing FMCW MIMO radar for far-field 3-D imaging," *IEEE Trans. Microw. Theory Techn.*, vol. 65, no. 9, pp. 3474–3484, Sep. 2017, doi: [10.1109/TMTT.2017.2661742](#).
- [28] J. Yan, G. Zhang, H. Hong, H. Chu, C. Li, and X. Zhu, "Phase-based human target 2-D identification with a mobile FMCW radar platform," *IEEE Trans. Microw. Theory Techn.*, vol. 67, no. 12, pp. 5348–5359, Dec. 2019, doi: [10.1109/TMTT.2019.2939523](#).

- [29] S. Wei et al., "3DRIED: A high-resolution 3-D millimeter-wave radar dataset dedicated to imaging and evaluation," *Remote Sens.*, vol. 13, no. 17, p. 3366, Aug. 2021.
- [30] B. Zhang, G. Xu, R. Zhou, H. Zhang, and W. Hong, "Multi-channel back-projection algorithm for mmWave automotive MIMO SAR imaging with Doppler-division multiplexing," *IEEE J. Sel. Topics Signal Process.*, vol. 17, no. 2, pp. 1–13, Mar. 2022, doi: [10.1109/JSTSP.2022.3207902](https://doi.org/10.1109/JSTSP.2022.3207902).
- [31] M. Jiang et al., "4D high-resolution imagery of point clouds for automotive mmWave radar," *IEEE Trans. Intell. Transp. Syst.*, pp. 1–15, Sep. 2023, doi: [10.1109/TITS.2023.3258688](https://doi.org/10.1109/TITS.2023.3258688).
- [32] J. Li, P. Li, P. Li, L. Tang, X. Zhang, and Q. Wu, "Self-position awareness based on cascade direct localization over multiple source data," *IEEE Trans. Intell. Transp. Syst.*, early access, pp. 1–9, Sep. 2022, doi: [10.1109/TITS.2022.3170465](https://doi.org/10.1109/TITS.2022.3170465).
- [33] G. Xu, B. Zhang, H. Yu, J. Chen, M. Xing, and W. Hong, "Sparse synthetic aperture radar imaging from compressed sensing and machine learning: Theories, applications, and trends," *IEEE Geosci. Remote Sens. Mag.*, vol. 10, no. 4, pp. 32–69, Dec. 2022, doi: [10.1109/MGRS.2022.3218801](https://doi.org/10.1109/MGRS.2022.3218801).
- [34] X. X. Zhu, N. Ge, and M. Shahzad, "Joint sparsity in SAR tomography for urban mapping," *IEEE J. Sel. Topics Signal Process.*, vol. 9, no. 8, pp. 1498–1509, Dec. 2015.
- [35] Y. Li and Y. Chi, "Off-the-grid line spectrum denoising and estimation with multiple measurement vectors," *IEEE Trans. Signal Process.*, vol. 64, no. 5, pp. 1257–1269, Mar. 2016, doi: [10.1109/TSP.2015.2496294](https://doi.org/10.1109/TSP.2015.2496294).
- [36] Z. Yang and L. Xie, "On gridless sparse methods for line spectral estimation from complete and incomplete data," *IEEE Trans. Signal Process.*, vol. 63, no. 12, pp. 3139–3153, Jun. 2015.
- [37] Y. Zhang, Q. Yang, B. Deng, Y. Qin, and H. Wang, "Experimental research on interferometric inverse synthetic aperture radar imaging with multi-channel terahertz radar system," *Sensors*, vol. 19, no. 10, p. 2330, May 2019, doi: [10.3390/s19102330](https://doi.org/10.3390/s19102330).
- [38] J. Lu, L. Zhang, S. Wei, and Y. Li, "Resolution enhancement for forwarding looking multi-channel SAR imagery with exploiting Space-Time sparsity," *IEEE Trans. Geosci. Remote Sens.*, vol. 61, 2023, Art. no. 5200617, doi: [10.1109/TGRS.2022.3232392](https://doi.org/10.1109/TGRS.2022.3232392).
- [39] L. A. Gorham and L.J. Moore, "SAR image formation toolbox for MATLAB," *Proc. SPIE*, vol. 7699, Apr. 2010, Art. no. 769906.
- [40] T. J. Kragh and A. A. Kharbouch, "Monotonic iterative algorithm for minimum-entropy autofocus," in *Proc. Adapt. Sensor Array Process. (ASAP) Workshop*, vol. 40, no. 4, Jun. 2006, pp. 1147–1159.
- [41] X. X. Zhu and R. Bamler, "Superresolving SAR tomography for multidimensional imaging of urban areas: Compressive sensing-based TomoSAR inversion," *IEEE Signal Process. Mag.*, vol. 31, no. 4, pp. 51–58, Jul. 2014, doi: [10.1109/MSP.2014.2312098](https://doi.org/10.1109/MSP.2014.2312098).



**Gang Xu** (Senior Member, IEEE) was born in Zaozhuang, China, in 1987. He received the B.S. and Ph.D. degrees in electrical engineering from Xidian University, Xi'an, China, in 2009 and 2015, respectively.

From 2015 to 2016, he was a full-time Post-Doctoral Research Fellow at the School of Electrical and Electronic Engineering, Nanyang Technological University, Singapore. He is currently a Full Professor at the State Key Laboratory of Millimeter Waves, School of Information Science and Engineering, Southeast University, Nanjing, China. His research interests include synthetic aperture radar (SAR)/inverse SAR (ISAR) imaging and millimeter-wave radar.

Southeast University, Nanjing, China. His research interests include synthetic aperture radar (SAR)/inverse SAR (ISAR) imaging and millimeter-wave radar.



**Yuzhi Chen** (Student Member, IEEE) was born in Chuzhou, China, in 1998. He received the B.S. degree in electrical engineering from the University of Electronic Science and Technology of China, Chengdu, China, in 2020, and the M.S. degree in radio engineering from Southeast University, Nanjing, China, in 2023.

His research interests include radar signal processing, array signal processing, and synthetic aperture radar.



**Ang Ji** (Student Member, IEEE) was born in Zaozhuang, China, in 2000. He received the B.S. degree in electronic information engineering from Xidian University, Xi'an, China, in 2022. He is currently pursuing the M.S. degree at the State Key Laboratory of Millimeter Waves, School of Information Science and Engineering, Southeast University, Nanjing, China.

His current research is focused on synthetic aperture radar imaging.



**Bangjie Zhang** (Student Member, IEEE) was born in Suzhou, China, in 1995. He received the B.S. degree in information engineering from Southeast University, Nanjing, China, in 2018, where he is currently pursuing the Ph.D. degree with the State Key Laboratory of Millimeter Waves.

His research interests include millimeter-wave radar systems, synthetic aperture radar tomography, and inverse synthetic aperture radar imaging.



**Chao Yu** (Senior Member, IEEE) received the B.E. degree in information engineering and the M.E. degree in electromagnetic fields and microwave technology from Southeast University (SEU), Nanjing, China, in 2007 and 2010, respectively, and the Ph.D. degree in electronic engineering from University College Dublin (UCD), Dublin, Ireland, in 2014.

He is currently a Professor with the State Key Laboratory of Millimeter Waves, School of Information Science and Engineering, SEU, and Purple Mountain Laboratories, Nanjing. His current research interests include microwave and millimeter-wave power amplifier modeling and linearization, and 5G massive multiple-input–multiple-output (MIMO) radio frequency (RF) system design.



**Wei Hong** (Fellow, IEEE) received the B.S. degree in radio engineering from the University of Information Engineering, Zhengzhou, China, in 1982, and the M.S. and Ph.D. degrees in radio engineering from Southeast University, Nanjing, China, in 1985 and 1988, respectively.

In 1993, he joined the University of California at Berkeley, Berkeley, CA, USA, as a short-term Visiting Scholar. From 1995 to 1998, he was a short-term Visiting Scholar with the University of California at Santa Cruz, Santa Cruz, CA, USA.

Since 1988, he has been with the State Key Laboratory of Millimeter Waves, Southeast University, where he has been the Director since 2003. He is currently a Professor with the School of Information Science and Engineering, Southeast University. He has authored or coauthored over 300 technical publications and authored two books. His current research interests include numerical methods for electromagnetic problems, millimeter-wave theory and technology, antennas, electromagnetic scattering, and radio frequency (RF) technology for mobile communications.

Dr. Hong was an Elected IEEE MTT-S AdCom Member from 2014 to 2016. He is a Fellow of Chinese Institute of Electronics (CIE). He was a recipient of the National Natural Prizes twice and the First-Class Science and Technology Progress Prizes thrice issued by the Ministry of Education of China and Jiangsu Province Government, and the Foundations for China Distinguished Young Investigators and "Innovation Group" issued by the NSF of China. He is the Vice President of the CIE Microwave Society and the Antenna Society and the Chair of the IEEE MTTS/APS/EMCS Joint Nanjing Chapter. He served as an Associate Editor for IEEE TRANSACTIONS ON MICROWAVE THEORY AND TECHNIQUES from 2007 to 2010 and one of the guest editors for the 5G Special Issue of IEEE TRANSACTIONS ON ANTENNAS AND PROPAGATION in 2017.